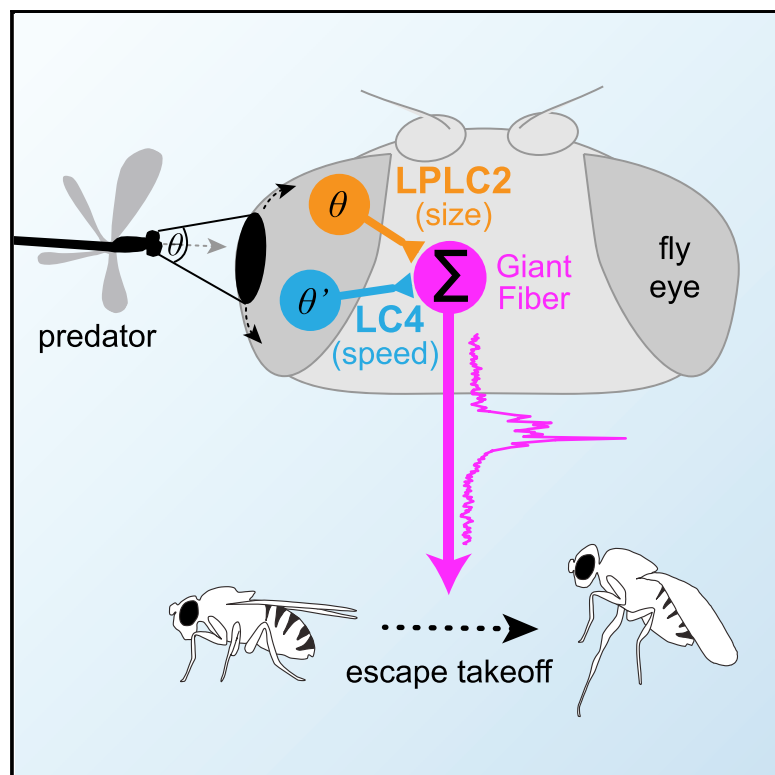


Current Biology

Neural Basis for Looming Size and Velocity Encoding in the *Drosophila* Giant Fiber Escape Pathway

Graphical Abstract



Authors

Jan M. Ache, Jason Polsky,
Shada Alghailani, ..., Davi D. Bock,
Catherine R. von Reyn,
Gwyneth M. Card

Correspondence
cardg@janelia.hhmi.org

In Brief

Ache et al. show that the *Drosophila* giant fiber descending neuron integrates synaptic input from LPLC2 and LC4 visual feature-detecting neurons to drive escape from approaching objects, such as an attacking predator. LPLC2 input to the giant fiber encodes the angular size of an approaching object, whereas LC4 input directly encodes looming speed.

Highlights

- LPLC2 and LC4 are the primary direct visual inputs to the giant fiber (GF)
- The GF sums LPLC2 and LC4 input to drive escape from looming
- LPLC2-GF input encodes looming size, whereas LC4-GF input encodes looming speed
- A model summing looming size and speed optical variables reproduces GF responses



Neural Basis for Looming Size and Velocity Encoding in the *Drosophila* Giant Fiber Escape Pathway

Jan M. Ache,¹ Jason Polksky,¹ Shada Alghailani,¹ Ruchi Parekh,¹ Patrick Breads,¹ Martin Y. Peek,¹ Davi D. Bock,^{1,4} Catherine R. von Reyn,^{2,3} and Gwyneth M. Card^{1,5,*}

¹Howard Hughes Medical Institute, Janelia Research Campus, Ashburn, VA 20147, USA

²School of Biomedical Engineering, Science and Health Systems, Drexel University, 3141 Chestnut Street, Philadelphia, PA 19104, USA

³Department of Neurobiology and Anatomy, Drexel University College of Medicine, 2900 W. Queen Lane, Philadelphia, PA 19129, USA

⁴Department of Neurological Sciences, Larner College of Medicine, University of Vermont, 149 Beaumont Avenue, Burlington, VT 05405, USA

⁵Lead Contact

*Correspondence: cardg@janelia.hhmi.org

<https://doi.org/10.1016/j.cub.2019.01.079>

SUMMARY

Identified neuron classes in vertebrate cortical [1–4] and subcortical [5–8] areas and invertebrate peripheral [9–11] and central [12–14] brain neuropils encode specific visual features of a panorama. How downstream neurons integrate these features to control vital behaviors, like escape, is unclear [15]. In *Drosophila*, the timing of a single spike in the giant fiber (GF) descending neuron [16–18] determines whether a fly uses a short or long takeoff when escaping a looming predator [13]. We previously proposed that GF spike timing results from summation of two visual features whose detection is highly conserved across animals [19]: an object's subtended angular size and its angular velocity [5–8, 11, 20, 21]. We attributed velocity encoding to input from lobula columnar type 4 (LC4) visual projection neurons, but the size-encoding source remained unknown. Here, we show that lobula plate/lobula columnar, type 2 (LPLC2) visual projection neurons anatomically specialized to detect looming [22] provide the entire GF size component. We find LPLC2 neurons to be necessary for GF-mediated escape and show that LPLC2 and LC4 synapse directly onto the GF via reconstruction in a fly brain electron microscopy (EM) volume [23]. LPLC2 silencing eliminates the size component of the GF looming response in patch-clamp recordings, leaving only the velocity component. A model summing a linear function of angular velocity (provided by LC4) and a Gaussian function of angular size (provided by LPLC2) replicates GF looming response dynamics and predicts the peak response time. We thus present an identified circuit in which information from looming feature-detecting neurons is combined by a common post-synaptic target to determine behavioral output.

RESULTS AND DISCUSSION

LPLC2 Visual Projection Neurons Are Required for Giant Fiber (GF)-Driven Escape Responses

LPLC2 (lobula plate/lobula columnar, type 2) neurons belong to a class of visual projection neurons whose outputs form optic glomeruli in the central brain [24, 25]. Each of the ~20 optic glomeruli is formed by axon terminals from one type of visual projection neuron, and different types are proposed to detect different visual features and feed into distinct motor pathways [24, 26–28]. One class of visual feature that is crucial for most animals to detect is looming, the rapid expansion of an object's image on the retina that signals the imminent threat of an approaching object, such as a predator. LPLC2 are implicated in the control of looming-evoked escape in *Drosophila*: they are strongly tuned to looming stimuli, their activation drives a fly to take off, and their silencing reduces takeoff rates in response to moderate looming speeds [22]. Whether and how LPLC2 contribute to the GF response to looming, however, is unclear.

To test whether LPLC2 are an integral part of the GF escape pathway, we silenced LPLC2 neurons and quantified the duration of the takeoff sequence evoked by a looming stimulus in unrestrained flies. *Drosophila* escape from looming stimuli by one of two different modes: a short-mode takeoff without prior wing movement that requires GF activation (Figure 1A) or a long-mode takeoff sequence of wing elevation followed by leg extension that does not require the GF [13, 30]. The short-mode takeoff lets flies escape a predator more quickly, whereas the long-mode takeoff is more stable, but takes longer to execute [13]. Using a high-throughput behavioral apparatus (FlyPEZ [31]), we quantified individual escape responses of 1,811 transgenic flies. LPLC2 neurons were genetically silenced using the GAL4-UAS system [32] with LPLC2-specific “split-GAL4” [33] promoters (“LPLC2,” Figures 1B–1D) driving expression of either TNT (tetanus toxin light chain) [34], a blocker of synaptic transmission, or Kir2.1 [35], a hyperpolarizing, inward-rectifying potassium channel. A driver line with the same genetic background but no expression in the nervous system (“Empty,” Figures 1B–1D) served as the control. Flies were shown looming stimuli that mimicked the constant-velocity approach of a predator [13]. For these stimuli, the time course of the visual angle subtended by the virtual object can be characterized by its size-to-velocity



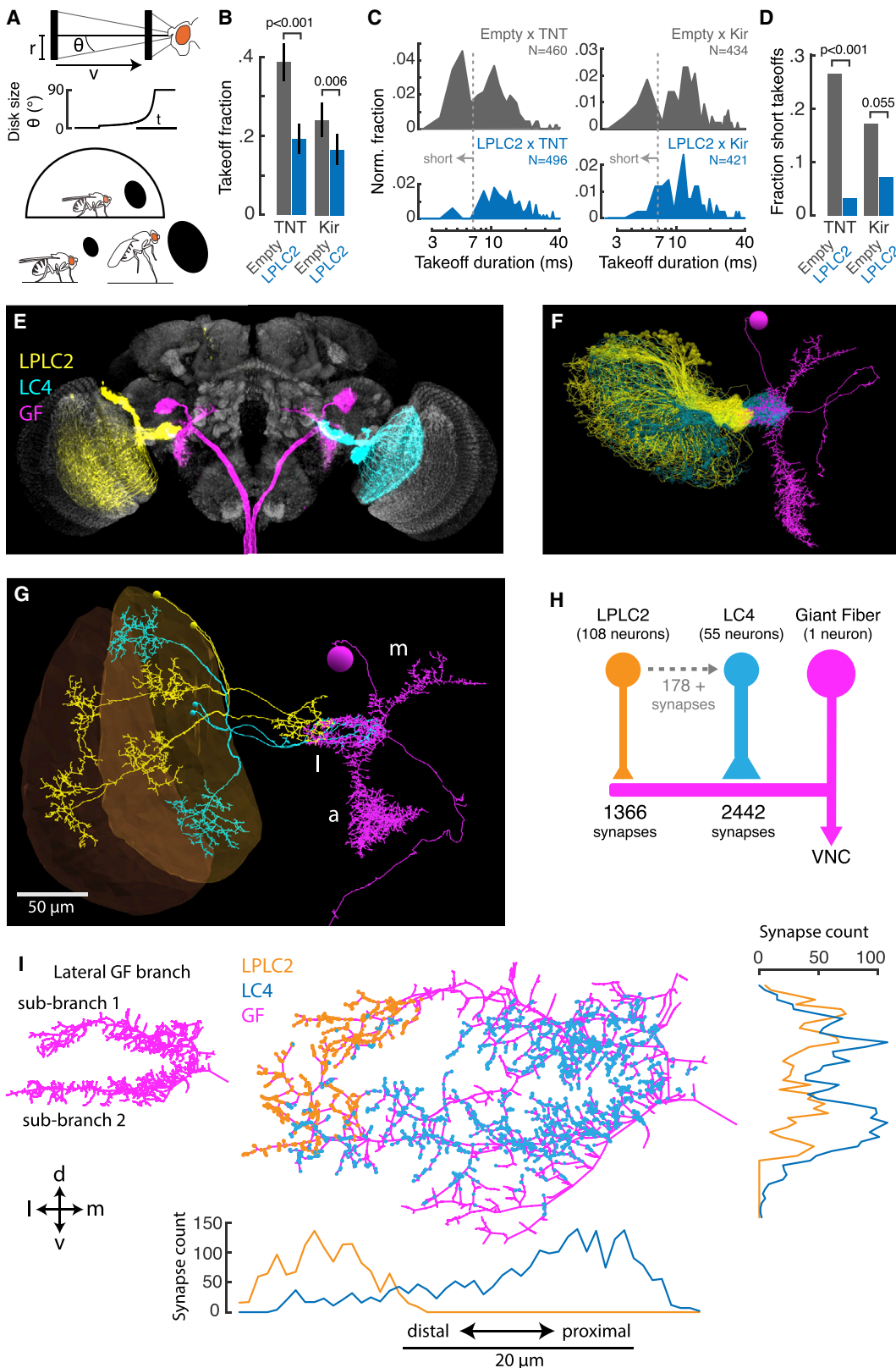


Figure 1. LPLC2 Are Required for GF-Mediated Escape Takeoffs and Synapse onto GF Dendrites

(A) Looming stimuli are the 2D retinal projection of a virtual object with radius, r , approaching the fly with constant velocity, v . r/v defines the dynamics of retinal angular disk size, θ , during expansion [29]. Individual flies respond to looming stimuli with a takeoff. The graphic shows the short-mode takeoff.

(legend continued on next page)

ratio (*r/v*, Figure 1A) [29]. Silencing LPLC2 with TNT or Kir reduced overall takeoff rates to looming stimuli (Figures 1B and S1) and almost completely abolished GF-mediated short-mode takeoffs (TNT: 26% [47/178] short-mode in control, 3% [3/93] in LPLC2-silenced flies; Kir2.1: 17% [18/105] control, 7% [5/70] LPLC2-silenced) (Figures 1C and 1D). We conclude that LPLC2 are required for GF-driven (short-mode) escape from looming stimuli, suggesting that LPLC2 neurons provide excitatory input to the GFs during looming.

LPLC2 and LC4 Visual Projection Neurons Are Directly Presynaptic to the GF

Synaptic contact from LPLC2 and LC4 (lobula columnar type 4) visual projection neurons to the GF was previously inferred from their overlap with GF dendrites in confocal microscopy images (Figure 1E) and from optogenetic activation of LPLC2 or LC4, which drove a short-latency GF depolarization [19, 22]. To confirm this connectivity and quantify synaptic inputs from LPLC2 and LC4, we reconstructed the complete GF and the axon terminals of the LPLC2 and LC4 populations in the right hemisphere of an adult *Drosophila* whole-brain electron microscopy volume [23] (Figure 1F; Video S1). LPLC2 and LC4 neurites were traced with enough detail to positively identify each neuron type [24]. The GF has three primary dendrites in the brain, which we label medial, lateral, and anterior (m, l, and a in Figure 1G). 55 LC4 and 108 LPLC2 neurons synapse directly onto the GF, exclusively at its lateral dendrite, forming a total of 2,442 LC4 and 1,366 LPLC2 synapses (Figure 1H; Video S2). These are more LPLC2 and fewer LC4 neurons than previously counted by confocal microscopy [24], suggesting that some LC4 neurons may not synapse onto the GF. Synapses from both cell types occurred on dorsal and ventral sub-branches of the lateral dendrite but segregated along the dendrite's distal-proximal axis, with LPLC2 synapses more distal, LC4 synapses more proximal, and interspersing of the two limited to small regions near the sub-branch tips (Figure 1I). Thus, LPLC2 and LC4 inputs are pooled on the same dendritic GF sub-branches but form a gradient along the distal-proximal axis.

Only six other visual projection neurons synapsed directly onto the GF, and these had relatively low synapse counts (1, 1, 3, 4, 6, and 8 synapses, respectively). Thus, LPLC2 and LC4 contribute 99.4% of the GF's direct-input synapses from the optic lobe. Unexpectedly, we also encountered synapses from LPLC2 directly onto LC4. Although it was not possible from our traced data to provide an accurate estimate of the numeric strength of the LPLC2 to LC4 connection, the relatively large number of synapses we identified serendipitously (>175) suggests that LPLC2 are a strong input to LC4.

Supralinear Summation of LPLC2 and LC4 Input Comprises the Excitatory GF Looming Response

We previously determined that LC4 input provides only one component of the excitatory GF response to looming objects [19]. We hypothesized that LPLC2 neurons, the only other visual projection neuron type strongly and directly connected to the GF, provide the remaining excitatory drive (Figure 2A). To test this, we performed experiments complementary to the previous LC4 silencing experiments [19]: recording GF looming responses via whole-cell patch clamp in LPLC2-silenced flies using the same setup and protocols (Figure 2B). To quantitatively compare results across the two studies, we used the LC11-silenced control data from [19] for our analysis, which matched, in form and amplitude, the control GF responses recorded in this study (Figure 2C and Figure S2). LC11 is not presynaptic to the GF (Figure 2A [19]), so LC11-silenced flies have an intact GF circuit and the same genetic background as experimental flies.

Looming stimuli evoke a complex GF response that, at the peak of depolarization, may result in a single spike (Figure 2C) sufficient to drive an escape jump. In LC11 × Kir control flies (Figure 2D, black), the looming onset drives a rapid transient GF depolarization. As the looming disk expands, the GF depolarizes gradually (Figure 2D, arrow E) but then repolarizes, ending with a tonic hyperpolarization (arrow F) that persists while the disk remains at maximum size (90°) and terminates with an inhibitory transient when the disk disappears (arrow G). Silencing LPLC2 significantly reduced excitatory GF responses to looming (Figure 2D) across all looming *r/v* values (Figure 2E), but it did not alter either the mean tonic hyperpolarization (Figure 2F) or off-transient peak (Figure 2G). These results suggest that LPLC2 contribute a large portion of the excitatory GF looming response, but they do not contribute to the inhibitory components.

To test our hypothesis that LPLC2 and LC4 constitute the only major excitatory inputs driving GF responses to looming stimuli, we summed the average GF response to a given looming stimulus measured in the LPLC2-silencing experiment with the average GF response to the same stimulus in the LC4-silencing experiment (from [19]) and compared the sum to the control response (Figure 2H). The sum of the two silencing experiments includes the following components: LPLC2 input (from the LC4-silencing experiments), LC4 input (from the LPLC2-silencing experiments), two times the tonic hyperpolarization component (one from each experiment), and two times any other excitatory or inhibitory inputs (Figure 2H, schematics on left). The residual from subtracting this sum from the control response, which includes each component once, represents any input that is not mediated by LC4 or LPLC2 (Figure 2H, schematics on left).

(B) Mean takeoff fraction \pm 95% confidence interval in control (empty \times TNT, empty \times Kir) and LPLC2-silenced (LPLC2 \times TNT, LPLC2 \times Kir) flies.

(C) Distribution of takeoff durations for flies in (B) normalized to total fly numbers; short-mode takeoffs have a duration of <6.87 ms [13].

(D) Fraction of short-mode takeoffs from distributions in (C). For (B)–(D), data were pooled across looming stimuli (*r/v* = 10, 20, 40, and 80), with *p* values from normal approximation to the binomial distribution.

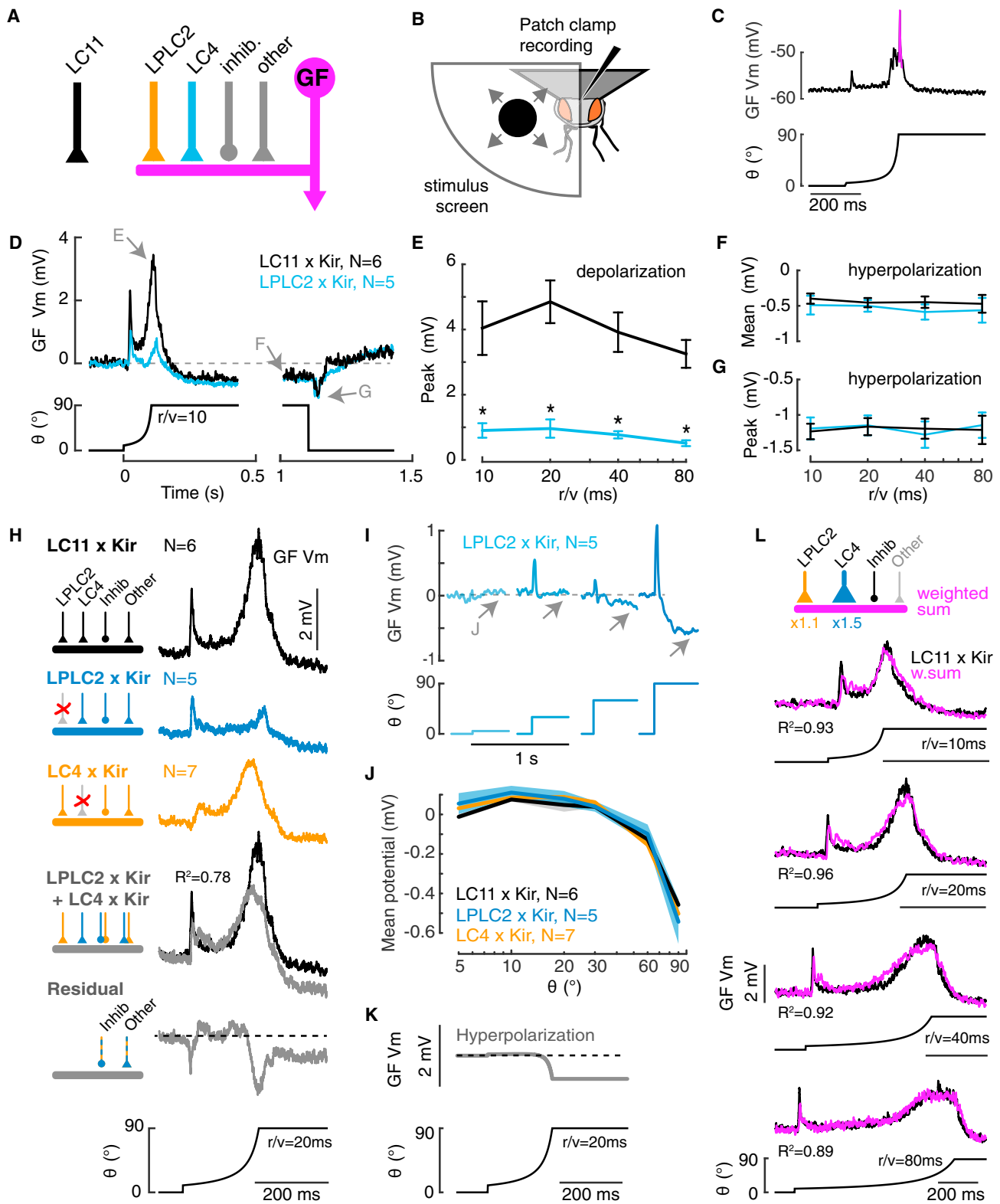
(E) Anterior view of overlaid right LPLC2 (yellow), left LC4 (cyan), both GFs (magenta), and brain neuropil (gray) from aligned light microscopy images.

(F) Electron microscopy (EM) reconstruction of neurons from (E) in the right brain hemisphere.

(G) Individual neuron reconstruction examples. Light orange, lobula; dark orange, lobula plate; m, medial; l, lateral; a, anterior GF dendrites.

(H) Connectivity diagram based on chemical synapses identified in EM. VNC, ventral nerve cord.

(I) Spatial distribution of LPLC2 and LC4 synapses on the lateral GF dendrite along the two main dendrite axes, distal-proximal (or lateral-medial, bottom) and dorsal-ventral (right). The left inset shows the two lateral GF sub-branches (magenta) after removal of central arborizations for visual clarity. d, dorsal; v, ventral; l, lateral; m, medial. See also Figure S1 and Videos S1 and S2.

**Figure 2. LPLC2 and LC4 Provide All Primary Excitatory Input to GF during Visual Looming**

(A) GF inputs contributing to looming include LPLC2, LC4, unknown inhibitory inputs contributing to the tonic hyperpolarization ("inhib."), and potentially other excitatory or inhibitory inputs ("other"). LC11 does not input to the GF and serves as a control.

(B) *In vivo* patch clamp set up for recording GF responses to looming stimuli.

(legend continued on next page)

The residual was negative or close to zero throughout the response, indicating that any additional input beyond LPLC2 and LC4 must be inhibitory and/or that the integration of LPLC2 and LC4 inputs is supralinear, such that concurrent activation of LPLC2 and LC4 in control flies results in stronger drive than do their separate activation in LC4/LPLC2-silenced flies.

We previously showed that the tonic hyperpolarization does not depend on LC4 because the size tuning of its amplitude in response to static disks is unchanged between control and LC4-silenced conditions [19]. To test if this component was similarly independent of LPLC2, we measured the GF response of LPLC2-silenced flies to static disks of different angular sizes that appeared and remained on the screen for 1 s (Figures 2I, S3A, and S3B). The amplitude of the resulting tonic hyperpolarization was size tuned, and it was nearly identical to that in LC4- and LC11-silenced flies (Figure 2J), confirming that the hyperpolarizing component derives from inhibitory GF input neurons independent from LPLC2 or LC4.

To determine whether a supralinear sum of LPLC2 and LC4 excitatory inputs plus the LPLC2/LC4-independent tonic hyperpolarization could account for the GF looming-response dynamics, we estimated the dynamics of the size-dependent hyperpolarization during looming (Figure 2K) by convolving the instantaneous stimulus disk size for a given looming stimulus with a fit to the average response to static disk presentations (Figure S3C). We next subtracted this estimated size-dependent hyperpolarization from the LPLC2-silenced and LC4-silenced GF response for each looming stimulus and used two-parameter least-squares approximations to find weights for the LPLC2 (the LC4-silenced response) and LC4 (the LPLC2-silenced response) components that best matched the mean control response across all *r/v* values tested (see STAR Methods). Use of optimal weights of 1.1 and 1.5 for the LPLC2 and LC4 components, respectively, fit the control data very well ($R^2 = 0.93 \pm 0.03$ across *r/v* values, Figure 2K). Thus, supralinear summation of LPLC2 and LC4 inputs can account for the entire excitatory drive to the GF during looming.

Supralinear summation during concurrent LPLC2 and LC4 activation could occur either within the GF's lateral dendrite or pre-synaptic to the GF. In particular, LPLC2 may increase LC4 visual responses via its synapses onto LC4 (Figure 1H) such that silencing LPLC2 indirectly decreases the drive from LC4 to the GF, which could explain why the LC4 component (LPLC2-silenced response) needed more weight than the LPLC2 component in the supralinear summation. Alternately, if Kir2.1 more

effectively silenced LPLC2 than LC4, we may have underestimated the LC4 contribution. This analysis strongly supports LPLC2 and LC4 as the two primary excitatory inputs contributing to the GF response to looming in the stimulus regime we explored.

The GF Receives Angular-Size Input from LPLC2 and Angular-Velocity Input from LC4 During Looming

Our previous analysis suggested that LC4 input to the GF encodes looming angular velocity as a high-pass filter, whereas the excitatory component remaining upon LC4 silencing encodes angular size in a non-monotonic fashion, such that the peak response occurs at a consistent angular-size threshold around 40° [19]. If LPLC2 and LC4 are the only excitatory looming inputs to the GF, then this non-LC4 component must derive from LPLC2 activity. This can be tested by silencing LPLC2 (the size component) and examining whether GF looming responses then depend only on angular velocity. The LPLC2-silenced GF membrane potential depolarization appeared to match the time course of looming angular velocity for each *r/v* ratio (Figure 3A). To measure if there was a consistent velocity-GF membrane-potential relationship across different stimuli, we plotted the instantaneous GF membrane potential against the instantaneous angular velocity for all looming stimuli. The relationship was well approximated for all *r/v* ratios ($R^2 = 0.66$) by a linear fit through the origin (Figure 3B), suggesting that LC4 input to the GF is directly proportional to the angular velocity of the looming stimulus. In contrast, there was no consistent relationship between the GF membrane potential and stimulus size after LPLC2 silencing (Figure 3C).

To directly measure the velocity tuning of the GF in LPLC2-silenced flies, we presented disks expanding with different, constant angular velocities (Figure 3D and Figure S3D). In these experiments, the GF peak depolarization also depended linearly on the angular velocity (Figure 3E). LPLC2 silencing reduced GF responses to slower angular velocities compared to controls (Figure 3F), whereas LC4 silencing specifically reduced GF responses to faster angular velocities ([19], Figure 3F). Furthermore, the slower velocity tuning in LC4-silenced flies matched the velocity tuning of individual LPLC2 neurons, which, though they encode looming size, require looming motion to be active [22]. Taken together, our results provide strong support for a model in which LPLC2 and LC4 provide complementary GF inputs, with LPLC2 providing the looming size and LC4 providing the looming velocity component.

(C) Example GF × GFP control response to a looming stimulus (*r/v* = 10 ms) with spike (magenta).

(D) Population-averaged GF looming responses in control LC11-silenced (LC11 × Kir) and LPLC2-silenced (LPLC2 × Kir) flies. Arrows and letters indicate response components quantified in subsequent panels.

(E) Peak (non-transient) depolarization during looming with different *r/v* values ($p < 0.005$ for each comparison).

(F–G) Mean tonic (F) and peak transient (G) hyperpolarization after looming stops during static presentation and disappearance of the 90° disk. All $p > 0.5$ (F) and > 0.3 (G). Plots in (E)–(G) show the mean \pm SEM, with *p* values from Wilcoxon's rank sum test. Colors are as in (D).

(H) Mean GF membrane potential in LC11 × Kir, LPLC2 × Kir, and LC4 × Kir flies (re-analyzed from [19]) during looming, with *r/v* = 20 ms. Diagrams on the left indicate which inputs were silenced in each experiment. Gray traces show the linear sum of LPLC2 × Kir and LC4 × Kir responses (top) and the residual response (bottom).

(I) LPLC2 × Kir GF response (top) to appearance of different angular sized disks (bottom). Arrows indicate the hyperpolarization analyzed in (J).

(J) Hyperpolarization during static disk presentation in LC11 × Kir, LPLC2 × Kir, and LC4 × Kir flies.

(K) Hyperpolarization component during looming estimated from fitting the data in (J).

(L) Weighted sum (magenta) of GF looming responses measured in independent experiments using LPLC2 × Kir and LC4 × Kir flies, minus the inhibitory component from (K), compared to GF control response (black). The UAS-Kir effector used for LPLC2 experiments in Figures 2 and 3 also contained transgenes to drive GFP expression in the GF for targeted patching ("GF-GFP_UAS-Kir," see STAR Methods). See also Figures S2 and S3.

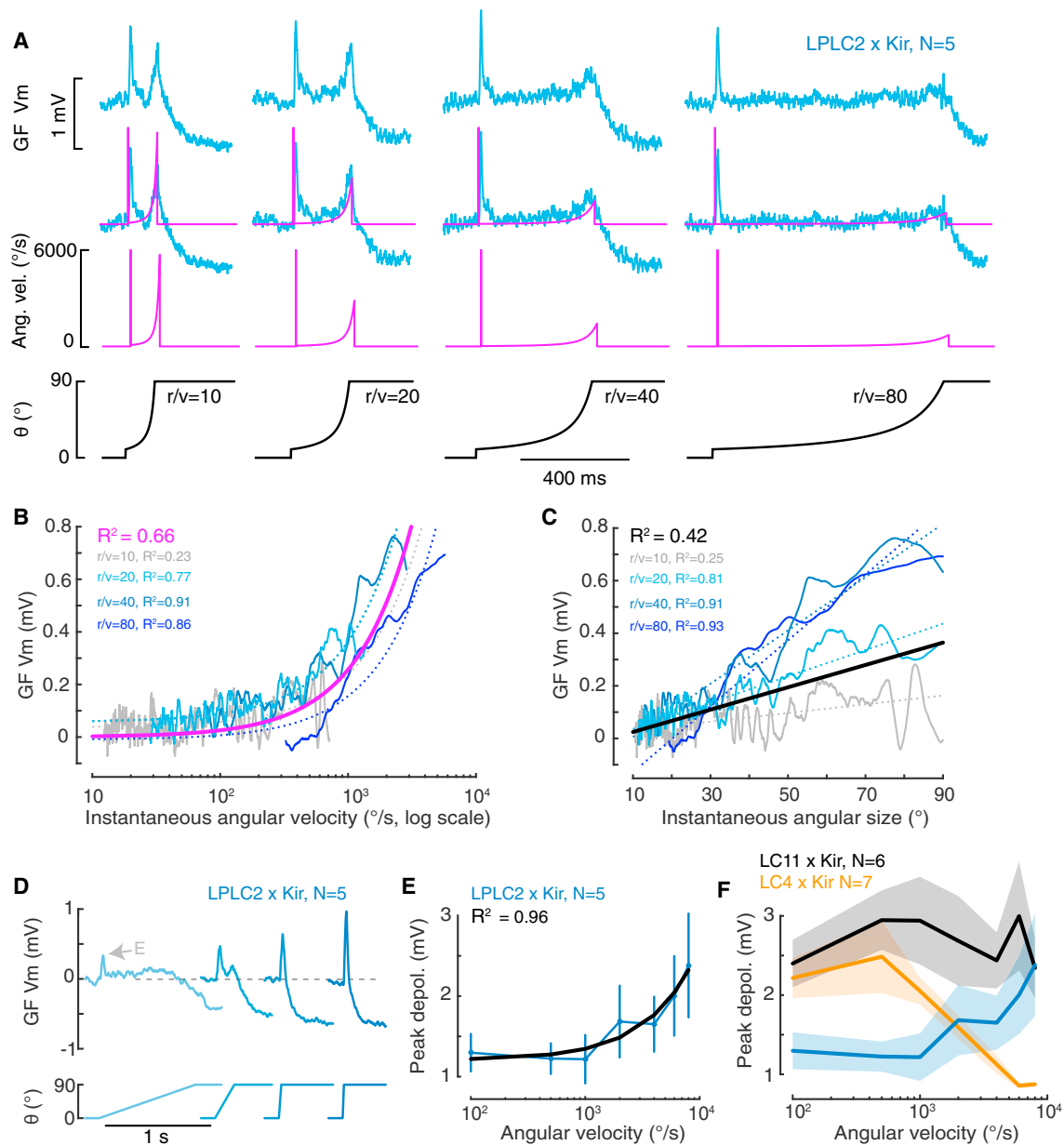


Figure 3. The GF Response Is Proportional to Looming Angular Velocity after LPLC2 Silencing

- (A) Mean LPLC2 × Kir GF response (blue) and instantaneous angular velocity (magenta) for looming stimuli with different r/v values. Velocity traces are only shown up to 6,000°/s and are time-shifted by 19 ms to account for GF latency.
- (B) Solid lines, mean LPLC2 × Kir GF response to looming stimuli with different r/v values plotted against instantaneous looming angular velocity. Dotted lines, linear fits for individual r/v values; magenta, linear fit to pooled data.
- (C) As in (B), but plotting GF membrane potential against instantaneous angular size. Black, linear fit to pooled data.
- (D) LPLC2 × Kir GF response (top) to objects expanding with different constant angular velocities (bottom).
- (E) Mean ± SEM peak depolarization (indicated in D) during constant velocity stimuli in (D). Black, linear fit.
- (F) Comparison of peak depolarization during constant-velocity looming stimuli for LC11 × Kir control (black), LC4 × Kir (orange, from [19]), and LPLC2 × Kir (blue) flies. Lines, mean; shading, SEM. See also Figure S3.

GF Responses Can Be Modeled by Summation of the Optical Variables ρ and η

There is remarkable convergence in which optical variables of looming stimuli are encoded across species. In particular, neurons encoding a retinal angular size threshold (η neurons) or angular expansion velocity (ρ neurons) have been found in

animals from insects to mammals [5–8, 11, 20, 21, 36]. We previously proposed that the GF looming response is comprised of ρ -like input from LC4 neurons and η -like input from an unknown source [19, 36]. Here, we establish that LPLC2 neurons comprise the unknown source and thus provide η -like input to the GF. Silencing LPLC2 allowed direct measurement of the LC4

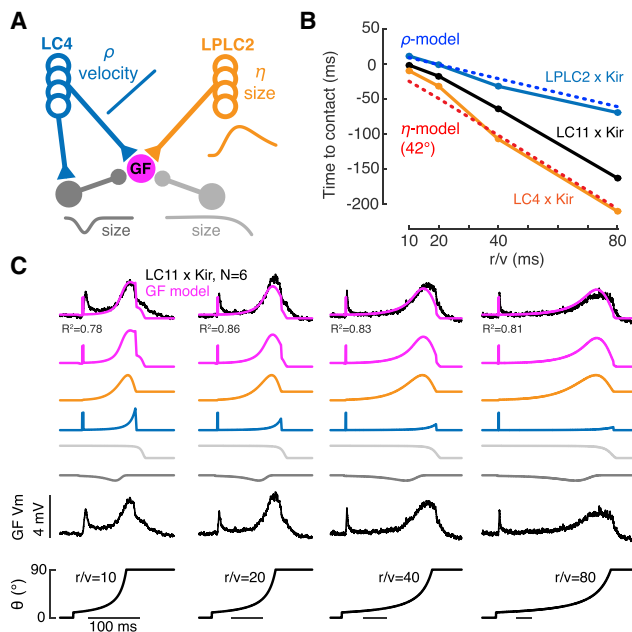


Figure 4. A Model Summing Looming Size and Velocity Matches the GF Looming Response

(A) A model (magenta) of GF input contributing to looming responses is composed of two excitatory components: ρ (a linear function of stimulus angular velocity, blue), and an η -like component (a Gaussian function of stimulus angular size with peak at 42°, orange), and two inhibitory components: an LC4- and LPLC2-independent tonic inhibition derived from a sigmoidal function of stimulus angular size (light gray, Figure 2J), and an LC4-dependent small-amplitude Gaussian function of stimulus angular size with peak at 25° (dark gray [19]). Each of the four components was estimated independently.

(B) Time of peak GF looming response across looming r/v values for LC11 x Kir control (black), LPLC2 x Kir (orange), and LC4 x Kir (blue) flies. Dashed lines, timing of peak response for model ρ neuron (blue) or model η neuron with size threshold 42° (red). GF peak responses are from population-averaged data. Time is relative to “time to contact” when the virtual object would reach a 180° subtended retinal angle.

(C) A weighted sum of the GF input model components (magenta) compared to the mean GF response in control flies for different r/v values. See also Figure S4.

contribution (Figure 3), and we determine that LC4 act as true ρ neurons, which have not previously been described in insects [20].

We thus propose that ρ - and η -like functions are summed supralinearly within (or just presynaptic to) the GF and that their summation determines the GF peak response time, when a spike driving the fly’s escape jump is most likely to occur (Figure 4A). To test this model, we compared peak GF response times across r/v values in control, LPLC2-silenced, and LC4-silenced flies (Figure 4B). A perfect ρ neuron’s peak response time is linearly related to the r/v ratio with a shallow slope (Figure 4B, blue dotted line), since the angular velocity peaks at the maximum stimulus size, in this case 90°. A perfect η neuron peaks at a particular threshold stimulus size, 42° in case of the GF η component [19], and so has a steeper linear relationship with r/v (Figure 4B, red dotted line). As predicted by our model, the control GF response, which is a combination of ρ - and η -like inputs, peaks

at times intermediate to those predicted by a perfect ρ or η neuron (Figure 4B, black). LC4 silencing (LPLC2 input only) shifts GF response times to match η predictions (Figure 4B, orange solid line), and LPLC2 silencing (LC4 input only) shifts GF response times to match ρ predictions (Figure 4B, blue solid line). In a further confirmation of this model, summing ρ - and η -like functions to predict the changes in GF membrane potential during a looming stimulus fit the time-course dynamics of the GF response across r/v values when we also include two empirically-measured inhibitory components: the tonic hyperpolarization at large disk sizes (Figures 2J and 2K) and a small, LC4-dependent hyperpolarization at small disk sizes (Figure 4C) (measured in [19]). This model also fit the GF response to non-looming stimuli, such as disks expanding at a constant velocity (Figure S4).

Since we can now attribute the GF size-tuned component to LPLC2, future experiments should derive the precise computation of this η -like component based on inherited properties from its T4/T5 motion-direction-selective input [22]. The tonic hyperpolarization inputs should also be identified. These have size tuning similar to that of inhibitory visual projection neuron inputs to a looming-sensitive neuron in the locust [37], but in *Drosophila*, the inhibitory inputs likely arise from interneurons receiving input from visual projection neurons, since we find few direct non-LC4/LPLC2 visual projection neuron synapses onto the GF. Interneurons may also provide additional excitatory input to the GF that provides visual information for non-looming stimuli not tested here.

Taken together, our results show how the response of a neuron driving escape jumps emerges from the summation of input from two cell types, LPLC2 and LC4 visual projection neurons, each of which represents a different classical model for looming detection (ρ and η). The GF circuit combines this angular size and speed information to determine GF spike timing in response to objects approaching on a collision course with different speeds, such as hunting predators. GF spike timing in turn dictates the timing of vital escape jumps and the choice of a short-mode or long-mode escape, which determines the probability of survival. Thus, action selection occurs directly postsynaptic to visual projection neurons in the *Drosophila* escape system, via integration of two different features of visual looming stimuli.

STAR★METHODS

Detailed methods are provided in the online version of this paper and include the following:

- KEY RESOURCES TABLE
- CONTACT FOR REAGENT AND RESOURCE SHARING
- EXPERIMENTAL MODEL AND SUBJECT DETAILS
 - Drivers
 - Effectors
- METHOD DETAILS
 - Light microscopy images
 - Neuron reconstruction in EM volume
 - Electrophysiology
 - Visual stimulation for electrophysiology
 - Behavioral experiments in the FlyPEZ
 - GF Model

- QUANTIFICATION AND STATISTICAL ANALYSIS
- DATA AND SOFTWARE AVAILABILITY

SUPPLEMENTAL INFORMATION

Supplemental Information can be found with this article online at <https://doi.org/10.1016/j.cub.2019.01.079>.

ACKNOWLEDGMENTS

We thank Scott Lauritzen for training in EM neuron tracing and tracing strategy; Srividya Murthy, Melissa Ryan, and Emily Tenshaw for help tracing and proofreading LPLC2 neurons; Chris Patrick, Andrew Champion, and Katharina Eichler for help with CATMAID; Aljoscha Nern for input on anatomy data; Grace Zheng for fly husbandry; the Janelia FlyLight Project Team for their contributions to generating data for Figure 1E; and Kit Longden and Card Lab members for comments on the manuscript. This study was supported by the Howard Hughes Medical Institute (HHMI).

AUTHOR CONTRIBUTIONS

J.M.A. acquired GF recordings, wrote the analysis and modeling code, analyzed data, made figures, wrote the paper, and designed experiments; J.P. and S.A. traced neurons; R.P. managed the tracing team; P.B. acquired FlyPEZ behavioral data; M.Y.P. generated genetic reagents and shared the visual stimulus code; D.B.B. acquired and shared the FAFB EM volume; C.R.vR. acquired GF recordings, wrote the analysis and modeling code, edited the paper, and designed experiments; and G.M.C. acquired funding, wrote the paper, designed experiments, and provided supervision.

DECLARATION OF INTERESTS

The authors declare no competing interests.

Received: November 15, 2018

Revised: January 18, 2019

Accepted: January 31, 2019

Published: February 28, 2019

REFERENCES

1. Hubel, D.H., and Wiesel, T.N. (1962). Receptive fields, binocular interaction and functional architecture in the cat's visual cortex. *J. Physiol.* **160**, 106–154.
2. Hubel, D.H., and Wiesel, T.N. (1968). Receptive fields and functional architecture of monkey striate cortex. *J. Physiol.* **195**, 215–243.
3. Maunsell, J.H.R., and Newsome, W.T. (1987). Visual processing in monkey extrastriate cortex. *Annu. Rev. Neurosci.* **10**, 363–401.
4. Zhao, X., Liu, M., and Cang, J. (2014). Visual cortex modulates the magnitude but not the selectivity of looming-evoked responses in the superior colliculus of awake mice. *Neuron* **84**, 202–213.
5. Shang, C., Liu, Z., Chen, Z., Shi, Y., Wang, Q., Liu, S., Li, D., and Cao, P. (2015). A parvalbumin-positive excitatory visual pathway to trigger fear responses in mice. *Science* **348**, 1472–1477.
6. Sun, H., and Frost, B.J. (1998). Computation of different optical variables of looming objects in pigeon nucleus rotundus neurons. *Nat. Neurosci.* **1**, 296–303.
7. Dunn, T.W., Gebhardt, C., Naumann, E.A., Riegler, C., Ahrens, M.B., Engert, F., and Del Bene, F. (2016). Neural circuits underlying visually evoked escapes in larval zebrafish. *Neuron* **89**, 613–628.
8. Liu, Y.J., Wang, Q., and Li, B. (2011). Neuronal responses to looming objects in the superior colliculus of the cat. *Brain Behav. Evol.* **77**, 193–205.
9. Hatsopoulos, N., Gabbiani, F., and Laurent, G. (1995). Elementary computation of object approach by a wide-field visual neuron. *Science* **270**, 1000–1003.
10. de Vries, S.E.J., and Clandinin, T.R. (2012). Loom-sensitive neurons link computation to action in the *Drosophila* visual system. *Curr. Biol.* **22**, 353–362.
11. Oliva, D., and Tomsic, D. (2014). Computation of object approach by a system of visual motion-sensitive neurons in the crab *Neohelice*. *J. Neurophysiol.* **112**, 1477–1490.
12. O'Carroll, D. (1993). Feature-detecting neurons in dragonflies. *Nature* **362**, 541–543.
13. von Reyn, C.R., Breads, P., Peek, M.Y., Zheng, G.Z., Williamson, W.R., Yee, A.L., Leonardo, A., and Card, G.M. (2014). A spike-timing mechanism for action selection. *Nat. Neurosci.* **17**, 962–970.
14. Seelig, J.D., and Jayaraman, V. (2013). Feature detection and orientation tuning in the *Drosophila* central complex. *Nature* **503**, 262–266.
15. Ziembka, C.M., and Freeman, J. (2015). Representing "stuff" in visual cortex. *Proc. Natl. Acad. Sci. USA* **112**, 942–943.
16. Levine, J., and Tracey, D. (1973). Structure and function of the giant motoneuron of *Drosophila melanogaster*. *J. Comp. Physiol.* **87**, 213–235.
17. Tanouye, M.A., and Wyman, R.J. (1980). Motor outputs of giant nerve fiber in *Drosophila*. *J. Neurophysiol.* **44**, 405–421.
18. Bacon, J.P., and Strausfeld, N.J. (1986). The dipteran "giant fibre" pathway: neurons and signals. *J. Comp. Physiol. A Neuroethol. Sens. Neural Behav. Physiol.* **158**, 529–548.
19. von Reyn, C.R., Nern, A., Williamson, W.R., Breads, P., Wu, M., Namiki, S., and Card, G.M. (2017). Feature integration drives probabilistic behavior in the *Drosophila* escape response. *Neuron* **94**, 1190–1204.e6.
20. Peek, M.Y., and Card, G.M. (2016). Comparative approaches to escape. *Curr. Opin. Neurobiol.* **41**, 167–173.
21. Laurent, G., and Gabbiani, F. (1998). Collision-avoidance: nature's many solutions. *Nat. Neurosci.* **1**, 261–263.
22. Klapoetke, N.C., Nern, A., Peek, M.Y., Rogers, E.M., Breads, P., Rubin, G.M., Reiser, M.B., and Card, G.M. (2017). Ultra-selective looming detection from radial motion opponency. *Nature* **551**, 237–241.
23. Zheng, Z., Lauritzen, J.S., Perlman, E., Robinson, C.G., Nichols, M., Milkie, D., Torrens, O., Price, J., Fisher, C.B., Sharifi, N., et al. (2018). A complete electron microscopy volume of the brain of adult *Drosophila melanogaster*. *Cell* **174**, 730–743.e22.
24. Wu, M., Nern, A., Williamson, W.R., Morimoto, M.M., Reiser, M.B., Card, G.M., and Rubin, G.M. (2016). Visual projection neurons in the *Drosophila* lobula link feature detection to distinct behavioral programs. *eLife* **5**, e21022.
25. Panser, K., Tirian, L., Schulze, F., Villalba, S., Jefferis, G.S.X.E., Bühl, K., and Straw, A.D. (2016). Automatic segmentation of *Drosophila* neural compartments using GAL4 expression data reveals novel visual pathways. *Curr. Biol.* **26**, 1943–1954.
26. Mu, L., Ito, K., Bacon, J.P., and Strausfeld, N.J. (2012). Optic glomeruli and their inputs in *Drosophila* share an organizational ground pattern with the antennal lobes. *J. Neurosci.* **32**, 6061–6071.
27. Sen, R., Wu, M., Branson, K., Robie, A., Rubin, G.M., and Dickson, B.J. (2017). Moonwalker descending neurons mediate visually evoked retreat in *Drosophila*. *Curr. Biol.* **27**, 766–771.
28. Ribeiro, I.M.A., Drews, M., Bahl, A., Machacek, C., Borst, A., and Dickson, B.J. (2018). Visual projection neurons mediating directed courtship in *Drosophila*. *Cell* **174**, 607–621.e18.
29. Gabbiani, F., Krapp, H.G., and Laurent, G. (1999). Computation of object approach by a wide-field, motion-sensitive neuron. *J. Neurosci.* **19**, 1122–1141.
30. Fotowat, H., Fayyazuddin, A., Bellen, H.J., and Gabbiani, F. (2009). A novel neuronal pathway for visually guided escape in *Drosophila melanogaster*. *J. Neurophysiol.* **102**, 875–885.
31. Williamson, W.R., Peek, M.Y., Breads, P., Coop, B., and Card, G.M. (2018). Tools for rapid high-resolution behavioral phenotyping of automatically isolated *Drosophila*. *Cell Rep.* **25**, 1636–1649.e5.

32. Brand, A.H., and Perrimon, N. (1993). Targeted gene expression as a means of altering cell fates and generating dominant phenotypes. *Development* 118, 401–415.
33. Luan, H., Peabody, N.C., Vinson, C.R., and White, B.H. (2006). Refined spatial manipulation of neuronal function by combinatorial restriction of transgene expression. *Neuron* 52, 425–436.
34. Sweeney, S.T., Broadie, K., Keane, J., Niemann, H., and O’Kane, C.J. (1995). Targeted expression of tetanus toxin light chain in *Drosophila* specifically eliminates synaptic transmission and causes behavioral defects. *Neuron* 14, 341–351.
35. Baines, R.A., Uhler, J.P., Thompson, A., Sweeney, S.T., and Bate, M. (2001). Altered electrical properties in *Drosophila* neurons developing without synaptic transmission. *J. Neurosci.* 21, 1523–1531.
36. Gabbiani, F., Krapp, H.G., Koch, C., and Laurent, G. (2002). Multiplicative computation in a visual neuron sensitive to looming. *Nature* 420, 320–324.
37. Wang, H., Dewell, R.B., Zhu, Y., and Gabbiani, F. (2018). Feedforward inhibition conveys time-varying stimulus information in a collision detection circuit. *Curr. Biol.* 28, 1509–1521.e3.
38. Namiki, S., Dickinson, M.H., Wong, A.M., Korff, W., and Card, G.M. (2018). The functional organization of descending sensory-motor pathways in *Drosophila*. *eLife* 7, e34272.
39. Pfeiffer, B.D., Truman, J.W., and Rubin, G.M. (2012). Using translational enhancers to increase transgene expression in *Drosophila*. *Proc. Natl. Acad. Sci. USA* 109, 6626–6631.
40. Nern, A., Pfeiffer, B.D., and Rubin, G.M. (2015). Optimized tools for multicolor stochastic labeling reveal diverse stereotyped cell arrangements in the fly visual system. *Proc. Natl. Acad. Sci. USA* 112, E2967–E2976.
41. Brainard, D.H. (1997). The psychophysics toolbox. *Spat. Vis.* 10, 433–436.
42. McDougal, R.A., Morse, T.M., Carnevale, T., Marenco, L., Wang, R., Migliore, M., Miller, P.L., Shepherd, G.M., and Hines, M.L. (2017). Twenty years of ModelDB and beyond: building essential modeling tools for the future of neuroscience. *J. Comput. Neurosci.* 42, 1–10.
43. Aso, Y., Hattori, D., Yu, Y., Johnston, R.M., Iyer, N.A., Ngo, T.T.B., Dionne, H., Abbott, L.F., Axel, R., Tanimoto, H., and Rubin, G.M. (2014). The neuronal architecture of the mushroom body provides a logic for associative learning. *eLife* 3, e04577.
44. Eichler, K., Li, F., Litwin-Kumar, A., Park, Y., Andrade, I., Schneider-Mizell, C.M., Saumweber, T., Huser, A., Eschbach, C., Gerber, B., et al. (2017). The complete connectome of a learning and memory centre in an insect brain. *Nature* 548, 175–182.
45. Saalfeld, S., Cardona, A., Hartenstein, V., and Tomančák, P. (2009). CATMAID: collaborative annotation toolkit for massive amounts of image data. *Bioinformatics* 25, 1984–1986.
46. Schneider-Mizell, C.M., Gerhard, S., Longair, M., Kazimiers, T., Li, F., Zwart, M.F., Champion, A., Midgley, F.M., Fetter, R.D., Saalfeld, S., and Cardona, A. (2016). Quantitative neuroanatomy for connectomics in *Drosophila*. *eLife* 5, e12059.
47. Maimon, G., Straw, A.D., and Dickinson, M.H. (2010). Active flight increases the gain of visual motion processing in *Drosophila*. *Nat. Neurosci.* 13, 393–399.
48. Lehnert, B.P., Baker, A.E., Gaudry, Q., Chiang, A.S., and Wilson, R.I. (2013). Distinct roles of TRP channels in auditory transduction and amplification in *Drosophila*. *Neuron* 77, 115–128.
49. Gouwens, N.W., and Wilson, R.I. (2009). Signal propagation in *Drosophila* central neurons. *J. Neurosci.* 29, 6239–6249.
50. Joesch, M., Weber, F., Eichner, H., and Borst, A. (2013). Functional specialization of parallel motion detection circuits in the fly. *J. Neurosci.* 33, 902–905.

STAR★METHODS**KEY RESOURCES TABLE**

REAGENT or RESOURCE	SOURCE	IDENTIFIER
Antibodies		
AF488 Goat anti Rabbit	Life Technologies	Thermo Fisher Scientific Cat# A-11034; RRID: AB_2576217
AF568 Goat anti Mouse	Life Technologies	Thermo Fisher Scientific Cat# A-11031; RRID: AB_144696
nc82 – Mouse anti bruchpilot	Developmental Studies Hybridoma Bank	DSHB Cat# nc82; RRID: AB_2314866
Rabbit polyclonal anti GFP Fraction	Life Technologies	Thermo Fisher Scientific Cat# A-11122; RRID: AB_221569
Experimental Models: Organisms/Strains		
'GF': R17A04_p65ADZp (attP40); 68A06_ZpGdbd (attP2)	[13]	SS_27721
'LPLC2': R19G02_p65ADZp (attP40); R75G12_ZpGdbd (attP2)	[24]	OL0048B
'LC4': R47H03_p65ADZp (attP40); JRC_SS00315 R72E01_ZpGdbd (attP2)	[24]	SS00315
'LC11': 22H02_p65ADZp (attP40); R20G06_ZpGdbd (attP2)	[24]	OL0015B
'Empty': R24A03-p65ADZp (attP40); R74C01-ZpGDBD (attP2)	[38]	SS01062
'Kir': pJFRC49-10XUAS-IVS-eGFPKir2.1 (attP2)	[13, 39]	n/a
'TNT': UAS-TNTe	[34]	n/a
'GFP': pJFRC28-10XUAS-IVS-GFP-p10 (attP2)	[39]	n/a
'GF-GFP_UAS-Kir': w; 68A06-LexAp65 (VK00022), pJFRC57-13LexAp2-IVS-GFP-p10 (su(Hw)attP5)/ (CyO); pJFRC49-10XUAS-IVS-eGFPKir2.1 (attP2)/ (TM6b)	this paper	n/a
10XUAS-IVS-myrl::smGFP-HA in attP18, 13LexAp2-IVS-myrl::smGFP-V5 in su(Hw)attP8	[40]	HA_V5
Software and Algorithms		
MATLAB	MathWorks	https://www.mathworks.com/
ImageJ	Rasband, W.S, National Institutes of Health	https://imagej.nih.gov/ij/
Psychophysics Toolbox	[41]	http://psychtoolbox.org
GF input model functions written in MATLAB	[19, 42]	ShowModel.cshtml?model=230400&file=/GF_loom_model/GF_loom_model.m#tabs-2">https://senselab.med.yale.edu/modeldb>ShowModel.cshtml?model=230400&file=/GF_loom_model/GF_loom_model.m#tabs-2
Other		
IHC protocols	FlyLight, Janelia Research Campus	https://www.janelia.org/project-team/flylight/protocols

CONTACT FOR REAGENT AND RESOURCE SHARING

Further information and requests for resources and reagents should be directed to and will be fulfilled by the Lead Contact, Gwyneth M. Card (cardg@janelia.hhmi.org).

EXPERIMENTAL MODEL AND SUBJECT DETAILS

Drosophila melanogaster were reared on standard cornmeal fly food and kept at 22°C and 50% humidity on a 16-hour light/8-hour dark cycle throughout development. Fly driver lines were crossed with fly effector lines (see below) as indicated in each figure, and the 3-5 day old progeny used for experiments. To genetically silence LPLC2 and LC4 we used split-GAL4 [33, 39] driver lines, which were specific for the respective population of neurons. For behavioral experiments in Figure 1, the Empty [38] split-GAL4 line was used to generate genetic controls because it has no expression in the nervous system, but was constructed in the same way as the other

split-GAL4 lines. For the electrophysiology experiments in [Figures 2, 3, and 4](#), the LC11 split-GAL4 line was used to generate genetic controls because LC11 does not synapse onto the Giant Fiber [19], but still expresses in a visual projection neuron population.

The following parental fly lines were used to generate experimental flies for the data presented in this study:

Drivers

- ‘GF’: R17A04_p65ADZp (attP40); 68A06_ZpGdbd (attP2), (SS_27721 [13])
- ‘LPLC2’: R19G02_p65ADZp (attP40); R75G12_ZpGdbd (attP2), (OL0048B [24])
- ‘LC4’: R47H03_p65ADZp (attP40); JRC_SS00315 R72E01_ZpGdbd (attP2) (SS00315 [24])
- ‘LC11’: 22H02_p65ADZp (attP40); R20G06_ZpGdbd (attP2), (OL0015B [24])
- ‘Empty’: R24A03-p65ADZp (attP40); R74C01-ZpGDBD (attP2), (SS01062 [38])

Effectors

- ‘Kir’: pJFRC49-10XUAS-IVS-eGFPKir2.1 (attP2) [13, 39]
- ‘TNT’: UAS-TNTe [34]
- ‘GFP’: pJFRC28-10XUAS-IVS-GFP-p10 (attP2) [39]
- ‘GF-GFP_UAS-Kir’: w; 68A06-LexAop65 (VK00022), pJFRC57-13LexAop2-IVS-GFP-p10 (su(Hw)attP5)/(CyO); pJFRC49-10XUAS-IVS-eGFPKir2.1 (attP2)/(TM6b), (this paper)

Behavioral experiments in [Figure 1](#) used the LPLC2 and Empty split-GAL4 lines crossed to Kir or TNT. For LPLC2 x Kir GF recordings in electrophysiological experiments ([Figures 2, 3, and 4](#)), the GF-GFP_UAS-Kir recombinant was crossed to the LPLC2-split GAL4 line so that we could target the GFP-expressing GF soma. GF x GFP control recordings ([Figure 2C](#) and [Figure S1](#)) were performed using the GF split-GAL4 line crossed to GFP. GF recordings in [19] were mostly acquired using split-GAL4 driver lines without GFP expression in the GF. GFP expression does not affect GF responses ([Figure S2](#) [13]).

METHOD DETAILS

Light microscopy images

Light-microscopy images in [Figure 1E](#) were generated by overlaying registered and aligned z-projections of the brains from three different split-GAL4 lines (“LC4,” “LPLC2,” “GF,” as above) crossed to a 10XUAS-IVS-myR::smGFP-HA in attP18, 13LexAop2-IVS-myR::smGFP-V5 in su(Hw)attP8 reporter line and processed for anti-GFP staining. The protocols for staining can be found at <https://www.janelia.org/project-team/flylight/protocols>. Brains were aligned using the anti-Brp reference pattern, following previously published methods [43], and overlaid in ImageJ (W.S. Rasband, National Institutes of Health, Bethesda, MD; <https://imagej.nih.gov/ij/>). LPLC2 and LC4 expression is bilaterally symmetric, however, for clarity, we cropped the LPLC2 and LC4 images at the midline of the brain before overlaying them with GF, and thus show LPLC2 neurons from the right optic lobe and LC4 neurons from the left optic lobe only.

Neuron reconstruction in EM volume

We traced the GF, LPLC2, and LC4 neurons in the right hemisphere of a serial section transmission electron microscopy volume of the full adult female *Drosophila* brain (FAFB [23]) using previously published software and methods [44]. In brief, we traced individual neurons using the web-based CATMAID software (<https://catmaid.readthedocs.io/en/stable/> [45, 46]). The right-hemisphere GF was traced out to completion. We identified its inputs by tracing back all neurons that were presynaptic, based on previously-established criteria for a chemical synapse [23]. All LPLC2 and LC4 neurons presynaptic to the GF were traced out until they were unambiguously identifiable. Thus, we accounted for all LPLC2 and LC4 neurons that are presynaptic to the right GF. Neuron identity was confirmed by comparison of traced neurons to light-microscopy image stacks [24], in particular their input structure in the Lobula and Lobula Plate layers, and their projection patterns in the central brain. We also used landmarks within the EM volume from previous tracing efforts to aid identification. Histograms of synapse distributions were generated in MATLAB from three-dimensional synapse location coordinates exported from CATMAID. Synapse counts for LPLC2 onto LC4 are based on near-complete reconstruction of several LPLC2 and LC4 neurons.

Electrophysiology

GF recordings were performed using the same visual stimulus protocols, display system, and electrophysiology setup we used previously, such that the data presented here are directly comparable to previously published GF recordings in LC4-silenced flies [19]. We used previously described methods [13, 19, 47] for *in vivo* whole-cell patch clamp recordings in behaving flies. In brief, three to five day old female progeny of driver lines crossed to GF-GFP_UAS-Kir2.1 were cold-anesthetized at 4°C and mounted on a pyramidal fly holder using UV-glue. Their front legs were removed to eliminate interference with visual stimulation and recordings, and their antennae were glued to reduce mechanosensory GF inputs [48]. The brain was exposed in the region of the GF soma by opening a window in the cuticle of the posterior surface of the head capsule. The brain was continuously perfused with fly extracellular saline

during recordings (103 mM NaCl, 3 mM KCl, 5 mM *N*-Tris (hydroxymethyl)methyl-2- aminoethane-sulfonic acid, 8 mM trehalose, 10 mM glucose, 26 mM NaHCO₃, 1 mM NaH₂PO₄, 1.5 mM CaCl₂ and 4 mM MgCl₂, adjusted to 273–275 mOsm, pH 7.3), which was held at 22°C and bubbled with 95% O₂/5% CO₂ [13, 49]. We locally applied Collagenase (5% or 2.5% in extracellular saline) with a blunt patch-pipette to render the tissue over the GF soma penetrable and disrupt the perineural sheath. The right GF, which was ipsilateral to the visual stimulus spherical projection screen, was visually targeted via brief GFP excitation and recorded using thick-walled patch electrodes with tip-resistances between 4 and 8 MΩ filled with intracellular saline (140 mM potassium aspartate, 10 mM HEPES, 1 mM EGTA, 4 mM MgATP, 0.5 mM Na₃GTP, 1 mM KCl, 20 μM Alexa-568-hydrazide-Na, adjusted to 260–275 mOsm, pH 7.3). Recordings were accepted for analysis if a seal resistance ≥ 8 GΩ was achieved before breaking in, and if the resting membrane potential was below -55 mV. Recordings were acquired in current clamp mode with a MultiClamp 700B amplifier (Molecular Devices, Sunnyvale, CA), low-pass filtered at 10 kHz, and digitized (Digidata 1440A, Molecular Devices, Sunnyvale, CA) at 20 kHz. No holding current was injected throughout. Intracellular traces were not corrected for a 13-mV liquid junction potential.

Visual stimulation for electrophysiology

For visual stimulation, we used A DMD projector without a color wheel running at 360 Hz (developed by A. Leonardo and Lightspeed Design; model I WXGA 360, see [13] for details), controlled by MATLAB (Mathworks, Natick, MA) using the Psychophysics Toolbox [41]. Stimuli were back-projected at 768 × 768 resolution onto a 7-inch diameter hemisphere coated with back projection paint (ScreenGoo, Goo Systems Global, Ontario, Canada).

Dark on white looming disk stimuli were projected at 11° elevation and 50° azimuth relative to the fly's head position and expanded from 10° to 90°. For looming stimuli, the disk center remained constant while the disk radius increased nonlinearly over time according to a model based on an object approaching the fly at a constant velocity [29]:

$$\theta(t) = 2 \tan^{-1} \left(\frac{r}{vt} \right) \quad (1)$$

where $\theta(t)$ is the angular size of the stimulus (in radians), r/v is the half size to approach speed ratio (in ms), and $t = 0$ at the virtual time of contact, when the object would reach 180°, such that $t < 0$ during object expansion (See Figure 1A).

Constant angular velocity stimuli were generated using:

$$\theta(t) = v_a t \quad (2)$$

where $\theta(t)$ is the angular size of the stimulus, v_a is the angular velocity, and $\theta = 0$ at $t = 0$. All stimuli were corrected for distortion and irradiance differences due to projection. For additional wild-type GF control experiments in Figure 2B and Figure S1, looming disks were presented at 45° azimuth and 45° elevation and expanded from 5° to 90° with r/v values of 10, 40, 70, 100 and 140 ms. Each stimulus was presented three to four times. Visual stimuli were randomized, and the inter-stimulus interval was 10 s.

Behavioral experiments in the FlyPEZ

Videos of freely behaving flies responding to looming stimuli were recorded at 6000 Hz using the FlyPEZ high throughput behavioral assay [31]. In brief, 1,811 individual flies were released, one-by-one onto a 5 × 5 mm transparent platform and exposed to visual looming stimuli. Side and ventral views of each fly were recorded under 740 nm infrared illumination. Visual stimuli were presented on 6-inch diameter back projection coated domes, using the same projectors, software and parameters used for electrophysiology experiments. The domes covered 360° in azimuth and 120° in elevation of the fly's visual field. Fly position on the platform was tracked in real-time, and the looming stimulus was presented according to the fly's real-time azimuthal orientation. The final position (median and interquartile range) of the looming stimulus relative to the fly was 11° elevation (fixed), and 51 ± 15° azimuth for LPLC2 x TNT, 51 ± 12° azimuth for Empty x TNT controls, 51 ± 13° azimuth for LPLC2 x Kir, and 51 ± 12° azimuth for Empty x Kir controls. Looming disks expanded from 5° to 90°. A single looming stimulus was presented per fly, and the platform was cleared before release of the subsequent fly, if the stimulus did not elicit an escape jump. All experiments were performed during the ~4h-long activity peak before lights-off in the flies' light cycle. Takeoffs were scored automatically and inspected manually. Takeoff duration was annotated manually, by labeling the first frame of wing raising and the last frame of tarsal contact. The escape duration data was pooled across all looming stimulus r/v values.

GF Model

We previously proposed a model [19] to predict the change in GF membrane potential during looming stimuli by combining four input components derived from our analysis of GF recordings in LC4-silenced flies (LC4 x Kir). Here we test whether that model still holds if we replace the previous model's velocity component with a velocity component based on the LPLC2 x Kir response, which represents the excitation from LC4. Since the GF membrane potential in LPLC2-silenced flies depended linearly on the stimulus velocity (Figure 3B), this V_{LC4} component was a true angular velocity (ρ) encoder. We therefore approximated V_{LC4} with a scalar multiplied by the angular velocity (a linear function of angular velocity passing through the origin):

$$V_{LC4} = C_1 * \dot{\theta}(t - \delta_1) \quad (3)$$

To empirically determine C_1 , we fit a line through the origin to the mean LPLC2 x Kir response to looming across r/v values (see Figure 3B). The sensory delay (δ_1) was measured from the latency from the time of disk appearance to the transient GF response in LPLC2 x Kir GF recordings to, which was 19 ms (see Figure 3A), resulting in $C_1 = 0.0002567$ and $\delta_1 = 0.019$ s.

The remaining three model components were based on the previously proposed GF model [19]. The second component, V_{LPLC2} , was a Gaussian function of the instantaneous angular size ($\theta(t)$) conveyed to the GF via excitatory LPLC2 inputs:

$$V_{LPLC2} = C_2 e^{\frac{-(\ln[\theta(t-\delta_2)] - \ln[C_3])^2}{2C_4^2}} \quad (4)$$

For looming stimuli, this function had a similar shape as one that is composed from a multiplication of size and velocity functions [29], but, because the η function did not fit our results for linearly-expanding stimuli, we modeled the η -like curve empirically as a Gaussian fit to the mean GF looming response in LC4 x Kir flies, after shifting the data to account for a sensory delay (δ_2), which we here set to 19 ms to match δ_1 . The coefficients from the fit, as derived in [19], are $C_2 = 1.7$, $C_3 = 42$, $C_4 = 0.52$ and $\delta_2 = 0.019$ s. Like the η function, this Gaussian model still acts as a size-threshold encoder, predicting peak response when the looming stimulus reaches an angular size of 42°.

The third component was an angular size-dependent inhibitory component, V_{i1} , that produced a tonic hyperpolarization at the end of our looming stimuli, when the 90° disk remained on the screen. This component was unaffected by LC4 or LPLC2 silencing, indicating it derived from an independent input source. We modeled V_{i1} as a sigmoid fit to the mean GF response during static disk presentation, according to [19]:

$$V_{i1} = C_5 + C_6 / \left(1 + e^{\frac{-(\theta(t-\delta_3) - C_7)}{C_8}} \right) \quad (5)$$

With $C_5 = -0.53$, $C_6 = 0.59$, $C_7 = 66$, $C_8 = -11$ and $\delta_3 = 0.0375$ s.

A fourth, relatively small LC4-dependent inhibitory component V_{i2} was modeled based on a Gaussian fit to the LC4 component of the GF response to an 100°/s angular velocity stimulus with respect to the time delayed (δ_4) size of the stimulus, according to [19]:

$$V_{i2} = C_9 e^{\frac{-(\theta(t-\delta_4) - C_{10})^2}{2C_{11}^2}} \quad (6)$$

With $C_9 = -0.52$, $C_{10} = 26$, $C_{11} = 7.8$ and $\delta_4 = 0.011$ s, as derived in [19].

The final GF membrane potential (V_{GF} , see Figure 4C) was modeled as the weighted sum of all four components, following:

$$V_{GF} = W_{LPLC2} * V_{LPLC2} + W_{LC4} * V_{LC4} + W_{i1} * V_{i1} + W_{i2} * V_{i2} \quad (7)$$

With $W_{LPLC2} = 1.45$, $W_{LC4} = 1.62$, $W_{i1} = 2.27$ and $W_{i2} = 1$. Weights for LPLC and LC4 were determined by least-squares optimization (see Figures S4B and S4C), while the weights for the inhibitory components were adopted from [19]. The modeled GF response was smoothed using a 2.5-ms time window.

QUANTIFICATION AND STATISTICAL ANALYSIS

All data analysis was performed in MATLAB. Statistical tests used and p values are noted in the main text, the figures, or figure captions. GF responses were lowpass-filtered, using MATLAB's "smooth" function and a 10-ms sliding window. For peak-time estimates in Figure 4B, a 1-ms smoothing window was used. To estimate the tonic hyperpolarization during static disk presentation after looming stimuli (Figure 2F), the GF membrane potential was averaged over a 100-ms window starting at 1 s after stimulus onset. To estimate the tonic hyperpolarization in response to the stimulus set of appearing disks subtending different angular sizes, the GF membrane potential was averaged in a 200-ms window starting 200 ms after the disk appeared on the screen (Figure 2J). We only analyzed trials in which the GF did not fire an action potential, since postsynaptic sub-threshold membrane potential changes are indicative of the presynaptic drive [19, 50]. Previously published LC11 x Kir controls and LC4 x Kir raw data from [19] were re-analyzed using the same parameters used for LPLC2 x Kir flies, such that all datasets were directly comparable.

To determine whether a weighted sum of LPLC2 input (measured in LC4-silenced responses) and LC4 input (measured in LPLC2-silenced responses) replicated full GF responses (Figure 3I), we iterated through different weights for both silenced responses and subtracted any superfluous hyperpolarizing inhibitory components from their weighted sum before calculating the coefficient of determination, R^2 , relative to LC11 x Kir control responses for each set of weights. The optimal weight combination (largest R^2 -value) for both response components was determined for each looming r/v value separately, before weights were averaged across all r/v values to determine the final, optimal weights. R^2 -values reported in Figure 3 were calculated using the final optimal weights. For example, at the final optimal weights of 1.5 (LPLC2 x Kir) and 1.1 (LC4 x Kir), we subtracted the hyperpolarizing component 1.5 times from the LPLC2 x Kir response, and 1.1 times from the LC4 x Kir response, and then added one hyperpolarizing component back in. This way, optimal weights for LPLC and LC4 input were determined by least-squares optimization.

DATA AND SOFTWARE AVAILABILITY

The GF input model will be deposited to ModelDB [42]. Information about and requests for data can be directed to and will be fulfilled by the Lead Contact, Gwyneth M. Card (cardg@janelia.hhmi.org).